Steps of spermiogenesis in the ostrich (*Struthio camelus*)

J. T. Soley[1], · L. du Plessis[2], · M. Sutovsky[3], · P. Sutovsky [3,4,*]

[1] Department of Anatomy and Physiology, Faculty of Veterinary Science, University of Pretoria, Private Bag X04, Onderstepoort 0110, South Africa

[2] Electron Microscope Unit, Faculty of Veterinary Science, University of Pretoria, Private Bag X04, Onderstepoort 0110, South Africa

[3] Division of Animal Sciences, University of Missouri, Columbia, MO 65211, USA

[4] Departments of Obstetrics, Gynecology and Women's Health, University of Missouri, Columbia, MO 65211, USA

*Correspondence to: P. Sutovsky. Email: sutovskyp@missouri.edu

Abstract

Few studies describe the sequence of morphological events that characterize spermiogenesis in birds. In this paper, the clearly observable steps of spermiogenesis are described and illustrated for the first time in a commercially important ratite, the ostrich, based on light microscopy of toluidine blue-stained plastic sections. Findings were supplemented and supported by ultrastructural observations, PNA labeling of acrosome development, and immunocytochemical labeling of isolated spermatogenic cells. Spermiogenesis in the ostrich followed the general pattern described in non-passerine birds. Eight steps were identified based on changes in nuclear shape and contents, positioning of the centriolar complex, and acrosome development. Only two steps could be recognized with certainty during development of the round spermatid which contributed to the fewer steps recorded for the ostrich compared to that described in some other bird species. The only lectin that displayed acrosome reactivity was PNA and only for the first three steps of spermiogenesis. This suggests that organizational and/or compositional changes may occur in the acrosome during development and merits further investigation. Immunological labeling provided additional evidence to support the finding of previous studies that the tip of the nucleus in the ostrich is shaped by the forming acrosome and not by the microtubular manchette. To our knowledge, this is the first complete description of spermiogenesis in ostrich and one of few in any avian species. In addition to comparative reproduction and animal science, this work has implications for evolutionary biology as the reported germ cell features provide a bridge between reptile and ratite-avian spermatogenesis.

Keywords: Spermiogenesis; Ostrich; Ratites

Introduction

Determining the cellular associations observed in the seminiferous epithelium during spermatogenesis provides important information relevant to the reproductive health of the male animal (Aire 2003) and forms a "basis for studying how spermatogenesis is regulated and for estimating the duration of spermatogenesis and the daily rate of sperm production of an animal" (Lin et al. 1990). An important element in the process of staging the cycle of the seminiferous epithelium is an accurate assessment of the various steps of spermiogenesis (Jones and Lin 1993). This process of morphological transformation of the spermatid has been reported in numerous light microscopical studies, supplemented subsequently by ultrastructural data provided by transmission electron microscopy in a wide range of vertebrate species. The steps of spermiogenesis have been described, for example, in rodents (Clermont and Rambourg 1978; Leblond and Clermont 1952; Manandhar and Sutovsky 2007), domestic mammals (Cavazos and Melampy 1954; Clermont and Leblond 1955), marsupials (Lin and Jones 2000; Ricci and Breed 2005; Setchell and Carrick 1973), reptiles (Courtens 1985; Ferreira and Dolder 2003; Gribbins 2011; Saita et al. 1987), and primates, including man (Barth and Oko 1989; Clermont and Leblond 1955; Fawcett and Phillips 1969; Holstein 1976; Holt and Moore 1984).

Several papers have addressed morphological aspects of spermiogenesis in passerine and non-passerine birds (for comprehensive reviews, see Aire 2007, 2014). Particular attention has been paid to birds of commercial importance such as the chicken (Cavazos and Melampy 1954; Gunawardana 1977; Gunawardana and Scott 1977), turkey (Aire 2003), duck (Clermont 1958; Marchand 1977; Simoes et al. 2005), quail (Lin and Jones 2000; Lin et al. 1990), and guinea fowl (Abdul-Rahman et al. 2017; Aire et al. 1980), although other avian groups including doves (Mattei et al. 1972; Yasuzumi and Yamaguchi 1977), parrots (Lovas et al. 2012), and ratites (du Plessis and Soley 2016) have also been examined. Despite this apparent plethora of data on avian spermiogenesis, it has been emphasized that these studies are restricted to a limited number of species (Aire 2007, 2014, 2018) and that very few reports have detailed the complete sequence of changes that characterize this process (Aire 2007).

Central to the interpretation of the various stages of the cycle is the accurate identification of the steps or phases of spermiogenesis. These steps have been documented for a limited number of bird species using various methods such as PAS or H&E staining of paraffin wax sections, toluidine blue or methylene blue staining of plastic sections, transmission electron microscopy, or a combination of these techniques (Abdul-Rahman et al. 2017; Aire 2003; Aire et al. 1980; Akhtar et al. 2020; Cavazos and Melampy 1954; Clermont 1958; Gunawardana 1977; Gunawardana and Scott 1977; Lin and Jones 1993; Lin et al. 1990; Lovas et al. 2012; Marchand 1977; Sprando and Russell 1988). Based on these studies, 10 steps of spermiogenesis have been identified in the Pekin duck (Clermont 1958), 10 (Aire et al. 1980) or 11 in the guinea fowl (Abdul-Rahman et al. 2017; Aire et al. 1980), 12 in the Japanese quail (Lin and Jones 1993; Lin et al. 1990) and turkey (Aire 2003), 10 in the goose (Akhtar et al. 2020), 6 in the Barbary duck (Marchand 1977), and 10 (Gunawardana 1977), 7 (Sprando and Russell 1988), and 4 (Gunawardana and Scott 1977) in the fowl, respectively. Fourteen steps based on acrosome formation have also been reported in the fowl (Cavazos and Melampy 1954) and four basic steps in the cockatiel (Lovas et al. 2012). A passerine bird, the house sparrow (*Passer domesticus*), has also been studied and 6 steps of spermiogenesis identified (Goes and Dolder 2002). The lack of consensus on the number of steps of spermiogenesis may reflect species-specific phenomena or, as is graphically illustrated in the various studies on the domestic fowl, the degree to which morphological changes are recognized to constitute a definitive step in the process.

Ratites such as the ostrich, emu, and rhea are raised worldwide and form small but important farming enterprises in several countries. Although organized on a successful commercial basis, the South African ostrich industry is beset by varied production problems which culminate in low productivity. The situation is exacerbated by sporadic outbreaks of avian influenza which results in the culling of large numbers of birds and the concomitant loss of income and valuable genetic material. These factors contribute to the high economic risk experienced by ostrich farmers and the exclusion from the industry of financially hamstrung emerging farmers. One of the factors adding to this situation is the need to keep relatively large numbers of male birds for the sole purpose of breeding. Commercial breeder birds are often kept in colonies that may exceed 100 birds at a male to female ratio of 5:10 to 6:10 (Lambrechts et al. 2004). Additionally, this system makes it difficult to efficiently improve the genetic quality of farmed ostriches (Bonato et al. 2011; Cloete et al. 2008; Kawka et al. 2007). It has been suggested that the use of assisted reproductive technologies such as artificial insemination (AI) could address these limitations (Bonato et al. 2011; Cloete et al. 2008; Malecki et al. 2008). With this in mind, and to understand more about the reproductive biology of the male ostrich, it may prove useful to determine the stages of the spermatogenic cycle in this commercially important ratite to further optimize its production potential. Although a number of papers have addressed aspects of spermiogenesis in this bird species in some detail (du Plessis and Soley 2013, 2016; Soley 1994, 1996, 1997), and information presented on the steps of spermiogenesis based on a combination of light microscopical and ultrastructural observations (Soley and Groenewald 1999), no practical guide to the identification of the individual steps of spermiogenesis at the light microscopical level or illustrations of the process have been published. In this paper, the clearly observable steps of spermiogenesis in the ostrich are described for the first time and illustrated based on light microscopic observations of toluidine blue-stained tissue sections. These observations are supplemented by ultrastructural data and previously published information. To gain further insight into the cytological events characterizing early stages of spermiogenesis, a variety of lectins were employed to trace acrosome development. Immunofluorescent staining of the nucleus and tubulin-containing structures was additionally employed to complement ultrastructural observations of sperm head shaping during spermatid elongation.

Materials and methods

Tissue sample collection and processing

The testes of 10 sexually mature and active ostriches (*Struthio camelus*) were collected during the breeding season following slaughter at a commercial abattoir. Small blocks of tissue were removed from the testes and immediately fixed for 18–24 h in 4% phosphate-buffered glutaraldehyde (pH 7.4). Samples were post-fixed for 1 h in 1% osmium tetroxide and routinely prepared for transmission electron microscopy (TEM) (du Plessis and Soley 2013).

Histology

Semi-thin sections, approximately 300 nm thick (displaying a purple color), were cut with a Leica EM UC7 ultramicrotome using a diamond knife, collected on glass slides, routinely stained with 1% toluidine blue and mounted with a coverslip prior to viewing with an Olympus BX63 light microscope. Images of the seminiferous tubules were captured by using a $100 \times$ oil objective. The various steps of spermiogenesis were identified and, where appropriate, linear measurements (representing approximate values) made of salient features such as nuclear length and diameter, by using the Olympus cellSens Imaging Software (Olympus Corporation,

Tokyo, Japan). In each instance, 50 measurements were performed and expressed as the mean ± SD.

Electron microscopy

Immediately after semi-thin sections were cut, ultrathin sections (90 nm; light gold-colored) representing the same area of interest were cut and collected on copper grids for transmission electron microscopy (TEM). These sections were stained with lead citrate and uranyl acetate before being viewed in a Philips CM10 transmission electron microscope operated at 80 kV.

Immunofluorescence

Testicular tissue processing and labeling was performed as described previously (Sutovsky et al. 2004; Yi et al. 2007). Briefly, pieces of testicular tissue were fixed in 2% formaldehyde, deparaffinized, rehydrated, and incubated with a mixture of the FITC-conjugated lectin (*Arachis hypogaea*/peanut agglutinin/PNA-FITC; Invitrogen) and DNA stain DAPI (Molecular Probes/Invitrogen; 2.5 µg/ml) for 40 min at room temperature. After a wash in PBS, the labeled sections were overlaid with VectaShield antifade mounting medium (Vector Laboratories, Newark CA), covered with microscopy coverslips, and sealed with clear nail polish before examination under a Nikon Eclipse 800 epifluorescence microscope. Images were recorded by using a Retiga QI-R6 camera (Teledyne QImaging, Surrey, BC, Canada) operated by MetaMorph 7.10.2.240. software (Molecular Devices, San Jose, CA). Figure plates were contrast balanced and edited by using Adobe Photoshop 2022 (Adobe Systems, San Jose, CA). Techniques applied to perform immunofluorescence on whole mounted, isolated testicular cells followed a described protocol (Sutovsky 2004). Briefly, blocks of fresh testicular tissue immediately after necropsy were gently minced in Petri dishes with 38 °C warm TL Hepes medium, strained through a 53 µm pore size nylon Spectra mesh (Cole Parmer, Vernon Hills, IL) to remove cell clumps, and fixed in 2% formaldehyde in PBS for 40 min. Fixed and PBS-washed spermatozoa were allowed to settle on poly-l-lysine-coated microscopy coverslips and sequentially incubated with a blocking solution (40 min in 5% normal goat serum/NGS in PBS supplemented with 0.1% Triton-X-100), primary anti-tubulin TUBB antibody clone E7 from DSHB Iowa City IA (40 min, diluted 1:200 in labeling buffer containing PBS with 1% NGS and 0.1 TX-100) and secondary antibody, goat anti-mouse IgG-TRITC from Zymed (40 min; diluted 1:200 in labeling buffer supplemented with 5 µg/ml DNA stain DAPI), with 5 min washes in labeling buffer after primary and secondary antibody. Negative controls were generated by replacing the primary antibody with a non-immune mouse serum (Sigma) at equivalent immunoglobulin concentration. Coverslips with labeled cells were mounted on microscopy slides and imaged as described for tissue sections.

Results

General observations

Variability in the arrangement of the cellular components of the ostrich seminiferous epithelium was a feature of the seminiferous tubules observed by using all imaging techniques including labeling with DNA stain DAPI (Fig. 1). Based on the fluorescent double labeling of tissue sections of the seminiferous epithelium using DAPI and lectin PNA-FITC, it was also possible to discern the early steps of spermiogenesis revealed by the presence of either round acrosomal granules/vesicles or flattened acrosomes (Fig. 2). In some areas, particularly those corresponding to late steps of spermiogenesis, the epithelium presented an ordered appearance

with clearly defined columns/tufts of spermatogenic cells being present (see Fig. 2a, b). However, in other areas, the cellular arrangement appeared less organized, with apparent mingling of different steps of spermiogenesis (Fig. 2c–e), although this appearance may be attributed to an oblique plane of sectioning in the imaged seminiferous tubule cross sections.
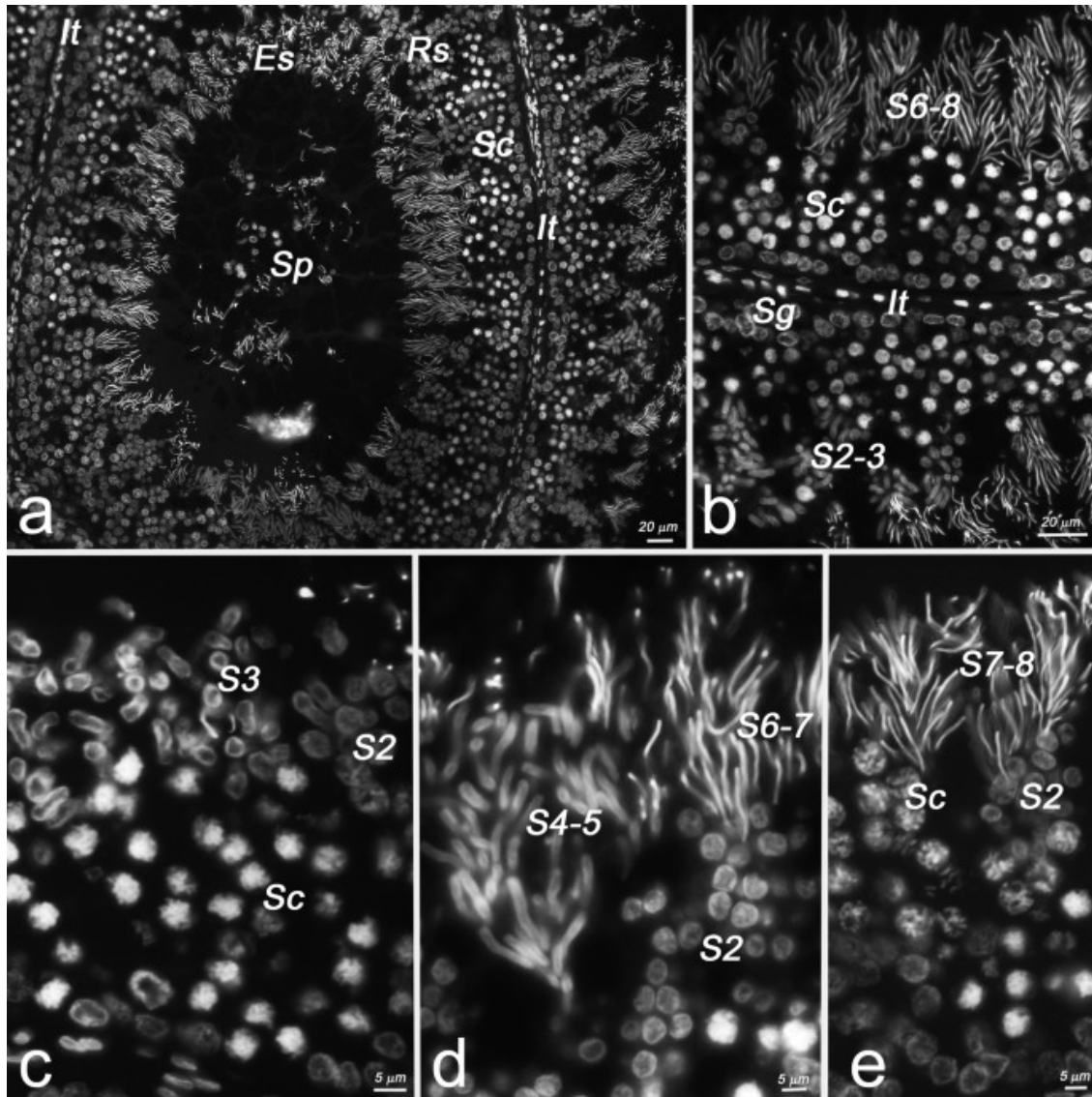

Fig. 1. Germ cell associations observed in paraffin sections of ostrich seminiferous epithelium stained with DNA stain DAPI. **a** Low-magnification view of a seminiferous tubule cross section shows an ordered arrangement of spermatid tufts, as well as all stages of spermiogenesis including round spermatids (Rs), elongated spermatids (Es), and spermiated spermatozoa in the tubule lumen (Sp). Adjacent tubules are separated by a layer of interstitial tissue (It) composed of myofibroblasts, specialized cells sharing the properties of smooth muscle cells and fibroblasts. **b** Detail of two adjacent tubules separated by interstitial tissue (It). Spermatogonia (Sg), spermatocytes (Sc), early step (S2-3), and late step (S6-8) elongating spermatids are discernible. **c–e** High-magnification images of adluminal seminiferous epithelium capturing the progression of meiosis and spermiogenesis from spermatocytes (Sc) to round (S2) and elongating (S3-8) spermatids
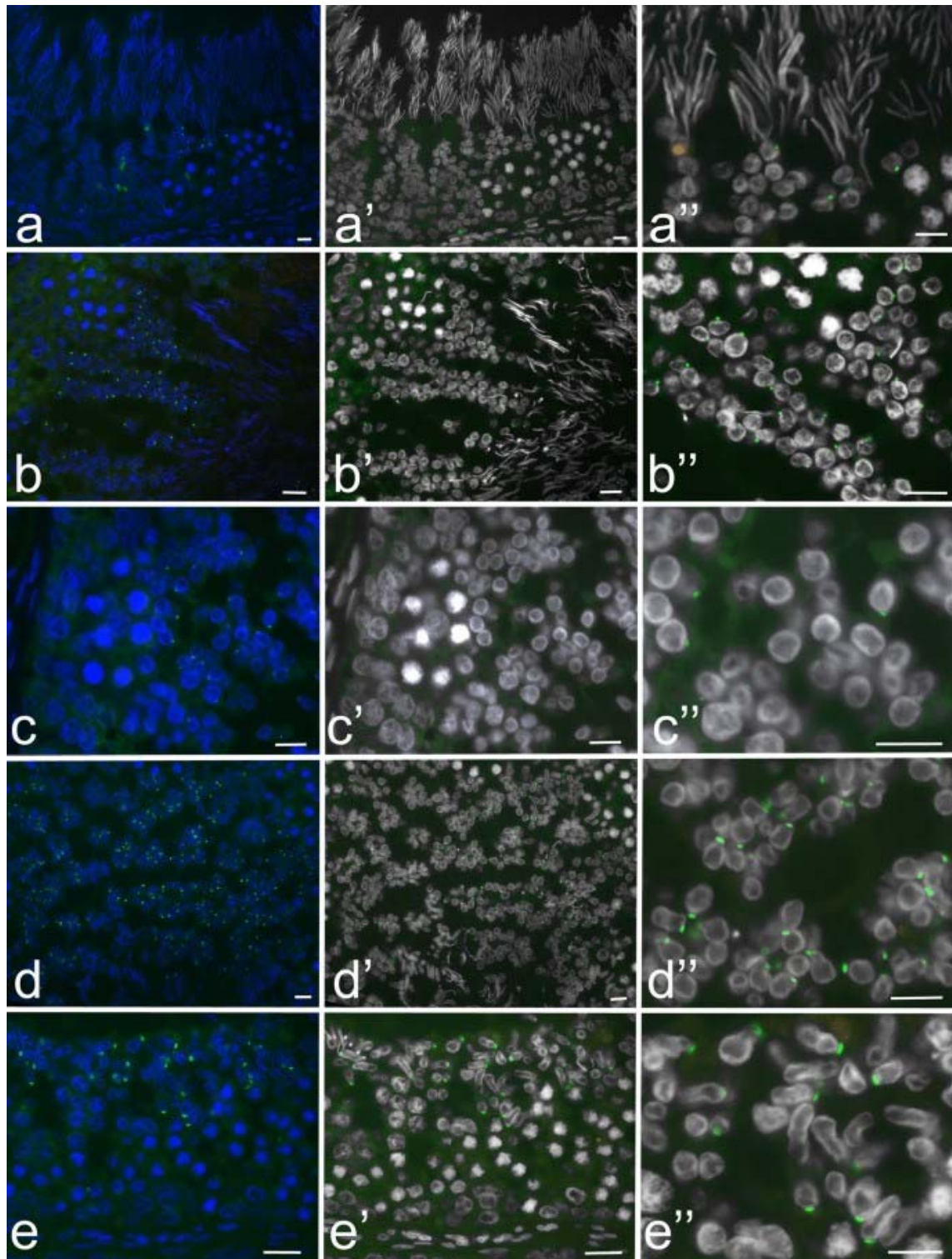
Fig. 2. Testis sections of the ostrich showing early stages of acrosome formation as revealed by PNA-FITC labeling (green color). Left column represents sections stained with DNA stain DAPI (blue) and lectin PNA-FITC (green) and the center column with DNA stain DAPI (grayscale) and lectin PNA-FITC (green). Right column shows enlargement of a selected area from the center column. **a–a″** Step 1 spermatids showing green labeling of the pro-acrosomal granules are shown in association with late elongating spermatids (step 7), free of acrosomal labeling. **b–b″** Step 1 spermatids associated with fully

elongated step 8 spermatids. **c, c″** Step 2 spermatids showing early stage of acrosomal granule flattening. **d–d″** Step 3 spermatids with flattened acrosomes and slightly elongated nuclei. **e–e″** Step 3 spermatids at a slightly later stage of development, with some cells displaying a gently convex acrosome and a more advanced stage of nuclear elongation. Note the ordered appearance of the seminiferous epithelium in **a** and **b** and the more disorganized arrangement in **c–e**. All scale bars = 10 µm

Based on the consistent appearance of specific cellular features, 8 steps of spermiogenesis could be identified with certainty in the ostrich. It should be emphasized that the morphological features for each step of spermiogenesis outlined below are based on scanning a group of closely related cells of similar appearance as single cells did not necessarily exhibit all the salient features of a particular step owing to the plane or depth of section. Transmission electron micrographs have been included where appropriate to illustrate morphological features not observed on LM or to corroborate descriptions. Basic ultrastructural characteristics are also provided, detailed descriptions of which have previously been published (du Plessis and Soley 2013, 2016; Soley 1994, 1996, 1997).

Steps of spermiogenesis

Step 1

Step 1 spermatids (Fig. 3a) were round cells with a spherical, centrally positioned nucleus and pale featureless cytoplasm. The nucleus, measuring 4.4 ± 0.29 µm in diameter, had a hazy appearance with interspersed clumps of chromatin, some of which were peripherally arranged. A pale homogeneous structure was often present in the center of the nucleus. One to three nucleoli were visible. Small dense structures could be seen in the vicinity of the nucleus in some cells possibly indicating the acrosomal granule and associated elements of the Golgi complex revealed by TEM (Fig. 3b). More prominent was the occurrence of a relatively large vesicle close to the nucleus which represented the acrosomal vesicle containing the dissipated contents of the acrosomal granule (Soley 1996). The presence of cytoplasmic vacuoles was a consistent feature of the developing spermatids and could not be distinguished from the acrosomal vesicle by light microscopy. Occasionally, some vacuoles lay against the nuclear membrane in both step 1 (Fig. 3b) and step 2 spermatids creating the erroneous impression that they represented the forming acrosomal vesicle. In such instances, the concentration of dense material at the point of contact between the vacuole and the nuclear envelope (see step 2) was not observed. The centriolar complex was generally situated close, and at a variable angle, to the nucleus. This structure was prominent due to the exceptionally long distal centriole (3 µm). In some cells, it was seen attached to the plasmalemma via a prominent annulus and extended into the intercellular space as the flagellum (Fig. 3a). The components of the forming acrosome and the centriolar complex remained unattached to the nuclear envelope during this phase and formed part of an organelle-rich concentration in the cytoplasmic lobe of the spermatid. TEM confirmed the light microscopic observations (Fig. 3b). In some cells, the centriolar complex and acrosomal granule vesicle were not obvious due to the plane of section, and nuclear size, shape, and structure were the identifying features of step 1 spermatids. Intercellular bridges were occasionally observed between neighboring spermatids during this step (Fig. 3a) and in all subsequent steps prior to spermiation.
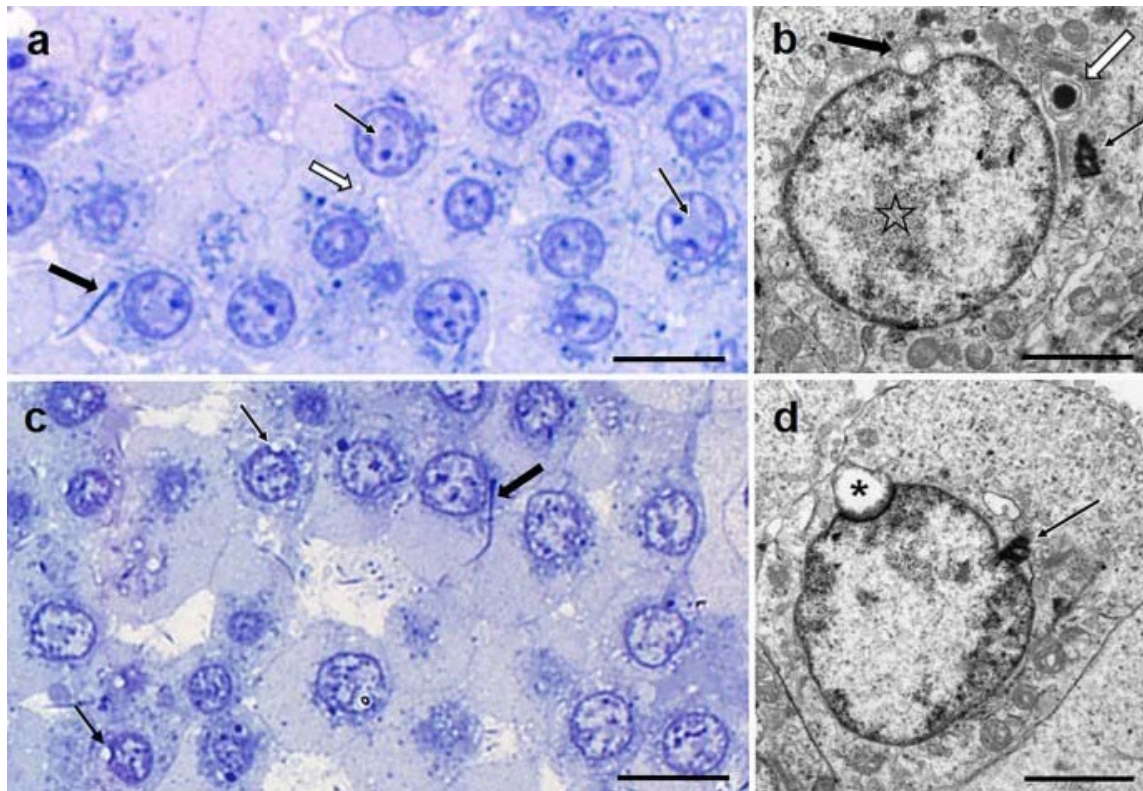
Fig. 3. Examples of step 1 (**a** and **b**) and step 2 (**c** and **d**) spermatids. **a** A group of step 1 spermatids. Note the hazy appearance of the nuclear contents, the pale central body (thin arrows), and the presence of nucleoli. The centriolar complex (thick arrow) and presumptive acrosomal granules/vesicles lie free in the cytoplasm. An intercellular bridge can be seen between two spermatids (white arrow). **b** TEM of a step 1 spermatid. The developing acrosomal granule surrounded by elements of the Golgi apparatus (white arrow) lies near the centriolar complex (thin arrow). The pale region seen in the nucleus on LM is represented by a collection of finely granular nuclear material (star). Note the erroneous impression created by a cytoplasmic vacuole that it is the attached acrosomal vesicle (thick arrow). **c** Step 2 spermatids. Note changes in the appearance of the nucleus and the attached acrosomal vesicles (thin arrows) and centriolar complex/flagellum (thick arrow). **d** TEM micrograph of a step 2 spermatid showing attachment of both the acrosomal vesicle (asterisk) and centriolar complex (arrow) to the nuclear envelope. The acrosomal vesicle lies in a densely lined nuclear crater with its contents concentrated along the nuclear aspect of the vesicle. Marginalization of the chromatin is apparent. Bars **a** and **c** = 4 μm; **b** and **d** = 2 μm

Step 2

Three obvious structural features differentiated this step from the previous step. (1) When present in the plane of section, the acrosomal vesicle was seen to have attached to the nuclear envelope forming a characteristic crater-like depression lined by a layer of dense material (Fig. 3c). This phenomenon was particularly obvious on TEM (Fig. 3d) which revealed that the dense layer seen by LM was formed by a narrowing of the nuclear envelope lining the floor of the crater, accentuated by a concentration of heterochromatin along the nuclear aspect and an accumulation of material on the floor of the acrosomal vesicle. Additionally, sandwiched between the membrane-bound wall of the acrosomal vesicle and the nuclear envelope was a layer of fine flocculant material representing the precursor of the sub-acrosomal component of the peri-nuclear theca (see Soley 1996 and du Plessis and Soley 2016). As in the previous step, the acrosomal vesicle appeared opaque due to the dispersion of its contents, although this

8

material was observed to concentrate at the point of contact with the nucleus, as noted above (Fig. 3d). (2) Attachment of the centriolar complex (diplosome/centrosome) to the nuclear envelope occurred in the vicinity of the acrosomal vesicle. During this phase, the attached acrosomal vesicle and centriolar complex were observed at varying distances from each other (Fig. 3d), in some instances being stationed at opposite poles of the nucleus. All other cytoplasmic features were similar to those of step 1 spermatids. (3) The nuclear contents displayed marked changes. Nucleoli were generally absent as was the pale central body. Clumps of dense heterochromatin were present, often interconnected by thread-like strands, and were separated by clear patches of euchromatin and nuclear matrix. Marginalization of the heterochromatin was an obvious feature of this phase. Nuclear diameter remained similar (4.2 ± 0.2 μm) to that in step 1 spermatids. Transitional stages demonstrating nuclear features of both step 1 and step 2 spermatids were also observed (Fig. 3c). Gradual and progressive collapse of the acrosomal vesicle, as well as flattening of the nuclear crater, was observed toward the end of this phase by TEM. As no specific morphological changes in the appearance of the centriolar complex and flagellum could be detected by LM following their initial formation and positioning during steps 1 and 2, these features could not be used as practical descriptors. The complex changes that occur in the nascent sperm tail connecting piece and flagellum of the developing spermatid (see (Soley 1994)) are therefore not described in this paper.

Step 3

The most obvious feature of this step was the change in nuclear shape that occurred. The round nucleus of steps 1 and 2 was seen to become pear-shaped (the most common shape), dumb-bell-shaped, or kidney-shaped (Figs. 4a and 5d). Initially, the nuclear contents displayed the same characteristics as the previous phase, but the chromatin gradually adopted a pale homogeneous appearance characteristic of step 4 spermatids. This change took place in the more constricted parts of the nucleus, spreading to the rest of the nucleus as narrowing progressed. The transformation of the nuclear contents between early and later step 3 spermatids was also obvious on TEM (Fig. 4b, c). Due to the variety of nuclear shapes, it was not possible to record accurate dimensions of nuclear diameter, but nuclear length was 6.52 ± 0.77 μm for this step. At the ultrastructural level, this step coincided with the initial development of the microtubule-based circular manchette typical of ratite spermiogenesis, which manifested as loose collections of microtubules oriented in a hoop-like fashion around the nucleus in the vicinity of the nuclear constrictions (Soley 1997). The forming acrosome and centriolar complex were positioned at opposite poles of the nucleus (Fig. 4a) with the latter generally being oriented parallel to the long axis of the cell (Fig. 4c). However, oblique attachment was sometimes observed. The acrosome appeared as a dense, flattened, dumb-bell-shaped or slightly convex structure closely invested by the plasma membrane (Fig. 4a–d). As revealed by TEM, this change in the shape and density of the forming acrosome resulted from progressive flattening of the acrosomal vesicle and the concentration of its contents. Invagination of the nuclear envelope from beneath the center of the developing acrosome resulted in the formation of the endonuclear canal and the accompanying acrosomal rod (perforatorium) (Fig. 4d) which, when fully developed, are typical features of mature ostrich spermatozoa (Soley 1996).
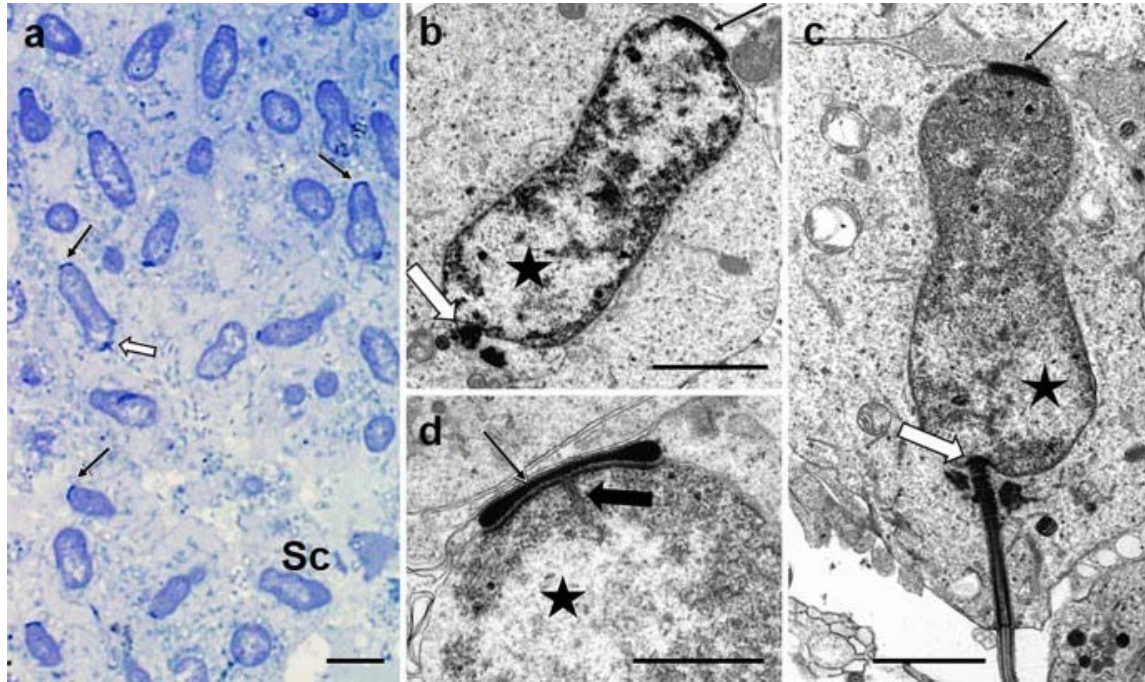
Fig. 4. Step 3 spermatids. **a** Light micrograph showing a group of advanced step 3 spermatids. Note the variability in nuclear shape although not as dramatic as in the beginning of this step and the lack of complete homogeneity of the chromatin, particularly in regions where the nucleus has not appreciably narrowed. Round/ovoid nuclear profiles represent transverse or oblique sections, and a single cell presents a scalloped nuclear profile (Sc). The forming acrosome presents as a dense flat or slightly convex structure capping the nucleus (arrows) and an attached centriolar complex can be seen in one cell (white block arrow). **b**–**d** TEM. **b** and **c** represent progressive stages in the development of step 3 spermatids based mainly on the increasing homogeneity of the nuclear contents although pale regions (stars) of less compacted material are a consistent feature. The cells in **a** and **c** are at a comparable stage of nuclear development. Flattened acrosome (arrows), centriolar complex (white arrows). **d** The forming endonuclear canal (thick black arrow) penetrates the karyoplasm from beneath the center of the developing acrosome (arrow). Bars **a** = 5 µm, **b** = 2 µm, **c** = 2 µm, **d** = 1 µm
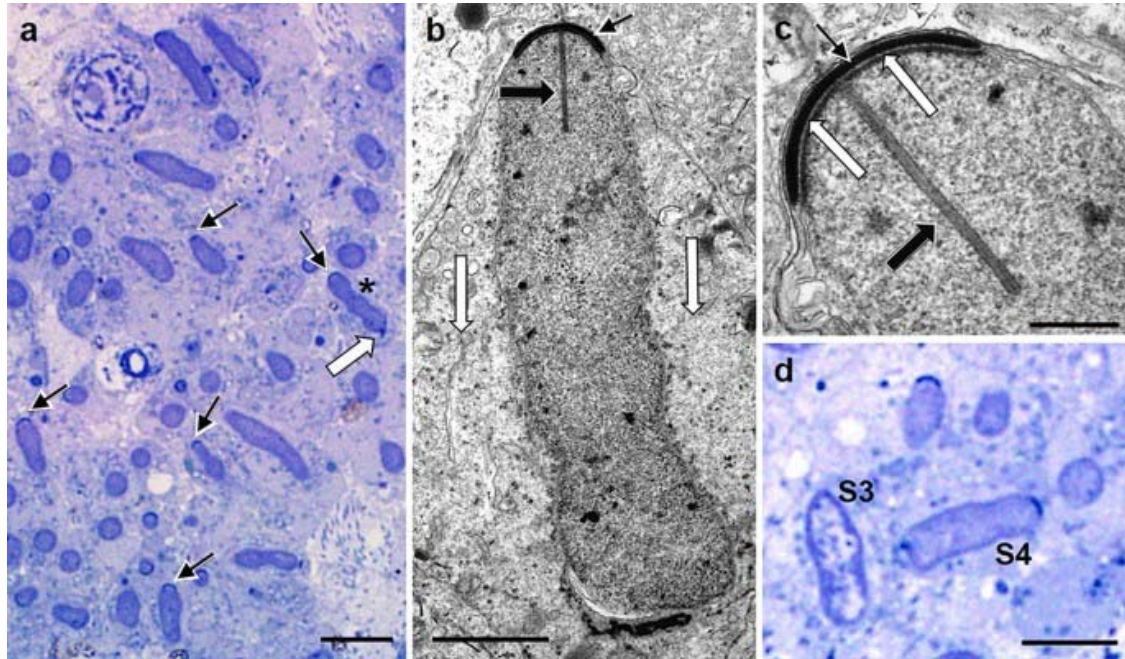
Fig. 5. Step 4 spermatids. **a** Light micrograph showing longitudinal and transverse profiles of step 4 spermatids. Although some nuclei have a slightly irregular appearance, they are all filled with fine, evenly distributed chromatin. The forming acrosome (arrows) and centriolar complex (white arrow) are visible in some cells. **b** TEM illustrating the crescent-shaped acrosome (thin arrow), the deepening endonuclear canal (thick arrow), and the finely granular, evenly distributed chromatin. Note the absence of any gaps in the karyoplasm during this phase and the caudal polarization of the cytoplasm (white arrows). This cell is similar to the one indicated with an asterisk in **a**. **c** Enlargement of the forming acrosome showing the relationship between the acrosome (thin black arrow), sub-acrosomal space (white arrows), and the endonuclear canal enclosing the acrosomal rod (thick black arrow). **d** LM comparing nuclear morphology between a step 3 (S3) and step 4 (S4) spermatid. Bar **a** = 8 μm, **d** = 6 μm, **b** = 2 μm, **c** = 0.5 μm

Step 4

Step 4 spermatids displayed a visibly elongated form (Fig. 5a, b, d) with signs of caudal polarization of the cytoplasm (Fig. 5b). The nucleus narrowed (diameter 2.75 ± 0.18 μm) and expanded to a length of 8.20 ± 0.66 μm, adopting an almost rectangular shape. Although the nucleus was more regular in shape, some spermatids displayed slightly misshapen nuclei as an indication of their earlier transformation. Scalloped forms were readily identified due to the presence of multiple constrictions. The chromatin was homogeneous and evenly distributed throughout the nucleus (Fig. 5a, d). The progressive changes in nuclear morphology from step 1 to step 4 were clearly defined and unambiguous (Fig. 6). The acrosome was convex to crescent-shaped and extended further around the tip of the nucleus in some cells. Basic TEM features included finely granular, homogeneous chromatin with scattered dense granules, a more organized circular manchette, deepening of the endonuclear canal, and concomitant lengthening of the acrosomal rod (Fig. 5b, c). The latter feature could not be observed on the light micrographs due to its delicate nature.
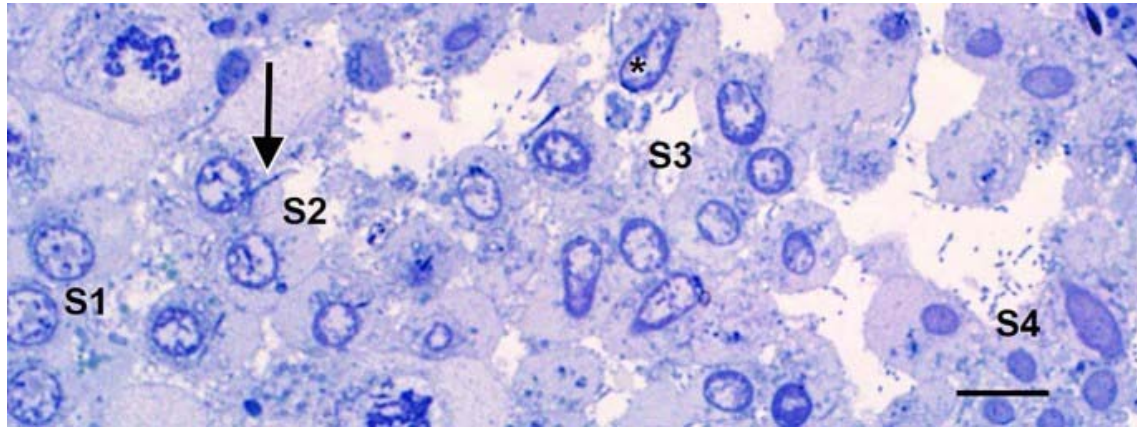
Fig. 6. Light micrograph illustrating the progressive changes in morphology between step 1 (S1), step 2 (S2), early step 3 (S3), and step 4 (S4) spermatids. Note the difficulty in assessing the steps of spermiogenesis based on acrosomal development alone, which, with one exception (asterisk), is not convincingly discernable in any of the cells. In this instance, nuclear shape and arrangement of the chromatin offer the pertinent criteria, although attachment of the centriolar complex (arrow) is typical for S2 spermatids. Bar = 4 μm

Step 5

The nuclei of step 5 spermatids were visibly longer (12.99 ± 1.54 μm) and narrower (1.71 ± 0.21 μm) than those of step 4 spermatids and exhibited a smooth, elongated profile with a consistent diameter. Although still homogeneous in appearance, there was a degree of marginalization of the chromatin resulting in a darker nuclear periphery and lighter center (Fig. 7a, b). TEM revealed that the finely granular chromatin of the previous phase was slowly transforming into a filamentous configuration with gaps in the karyoplasm appearing in the center of the nucleus (Fig. 7c, d). The forming filaments appeared granular in transverse sections (Fig. 7c). The acrosome adopted a more cone-shaped appearance and the fully developed circular manchette encircled the nucleus (Fig. 7c, d). In places, peculiar finger-like projections extended between the nuclear envelope and the manchette microtubules (du Plessis and Soley 2013, 2016).
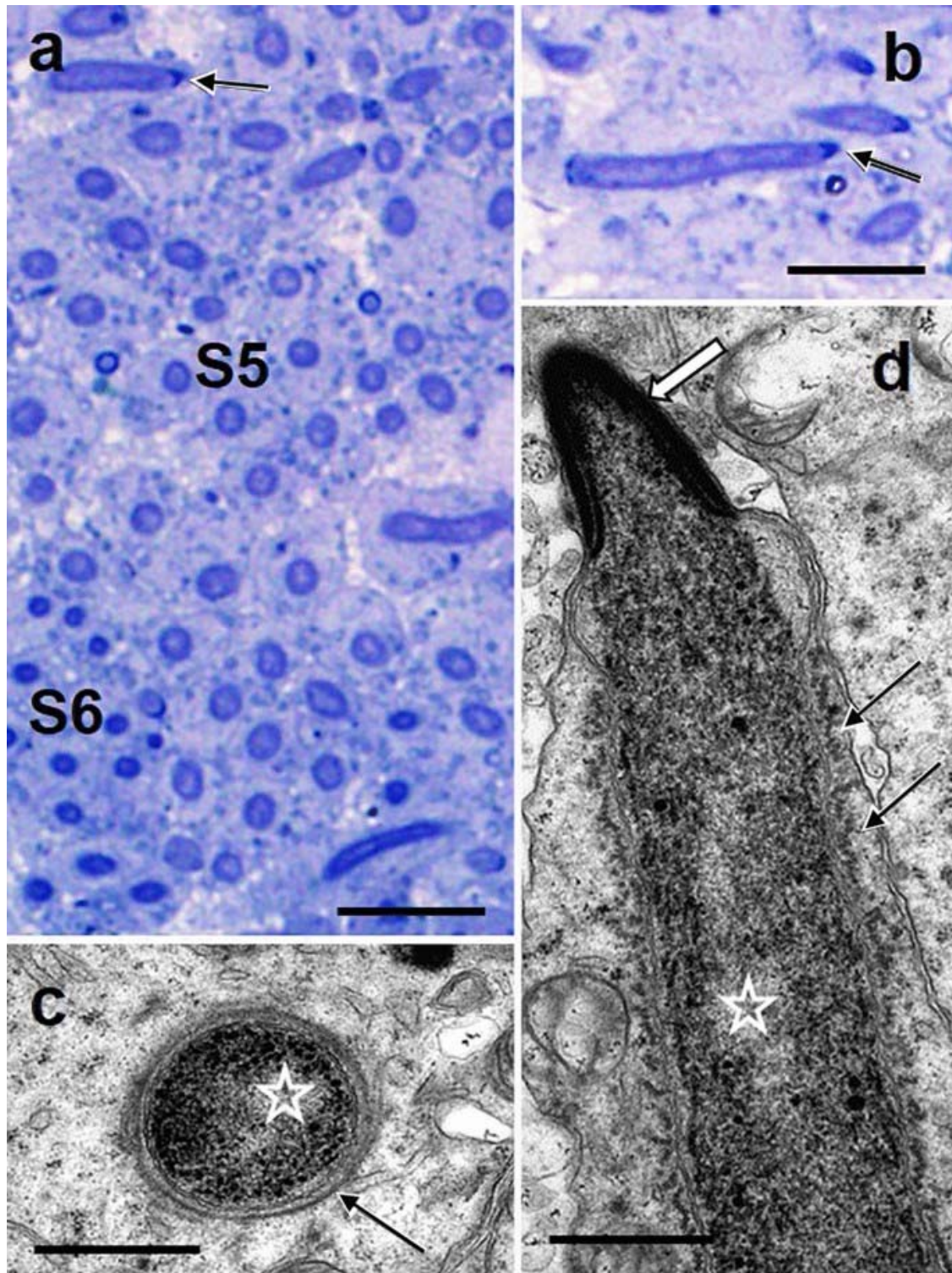
Fig. 7. Step 5 spermatids. **a** LM showing a large group of step 5 spermatids (S5) in transverse and longitudinal section. Note the smooth contours and darker periphery and lighter center of the nuclei. One cell displays a conical acrosome (arrow). Step 6 spermatids (S6). **b** Full length longitudinal profile of a step 5 spermatid. Cone-shaped acrosome (arrow). **c** and **d** TEM showing the more filamentous nature of the nuclear contents and a forming low-density space confined to the center of the nucleus (star) in transverse and longitudinal section, respectively. The fully developed circular manchette (black arrows) and conical acrosome (white arrow) are also illustrated. Bars **a** and **b** = 5 μm; **c** and **d** = 1 μm

13

Step 6

The most obvious morphological feature of step 6 spermatids was the increased elongation and narrowing (indicated by a nuclear diameter of 1.2 ± 0.17 μm) of the nucleus, accentuating the difference in staining intensity between the dark peripheral chromatin and the lighter staining center (Fig. 8a). The cells were capped by a cone-shaped acrosome. An obvious layer of cytoplasm remained around the nucleus except at the apex where the plasmalemma was tightly bound to the acrosome (Fig. 8b). On TEM, the karyoplasm demonstrated a peripheral collection of short, electron dense fibrils oriented along the long axis of the nucleus (Fig. 8b, c). The fibrils appeared as coarse dense granules in transverse section (Fig. 8d). The middle of the nucleus was filled with evenly distributed, finely granular material (Fig. 8b–d) evidently responsible for the pale nuclear centers seen by LM. The circular manchette was still evident (Figs. 8b–d), as were the randomly scattered finger-like projections (not illustrated here—see (du Plessis and Soley 2013, 2016)).
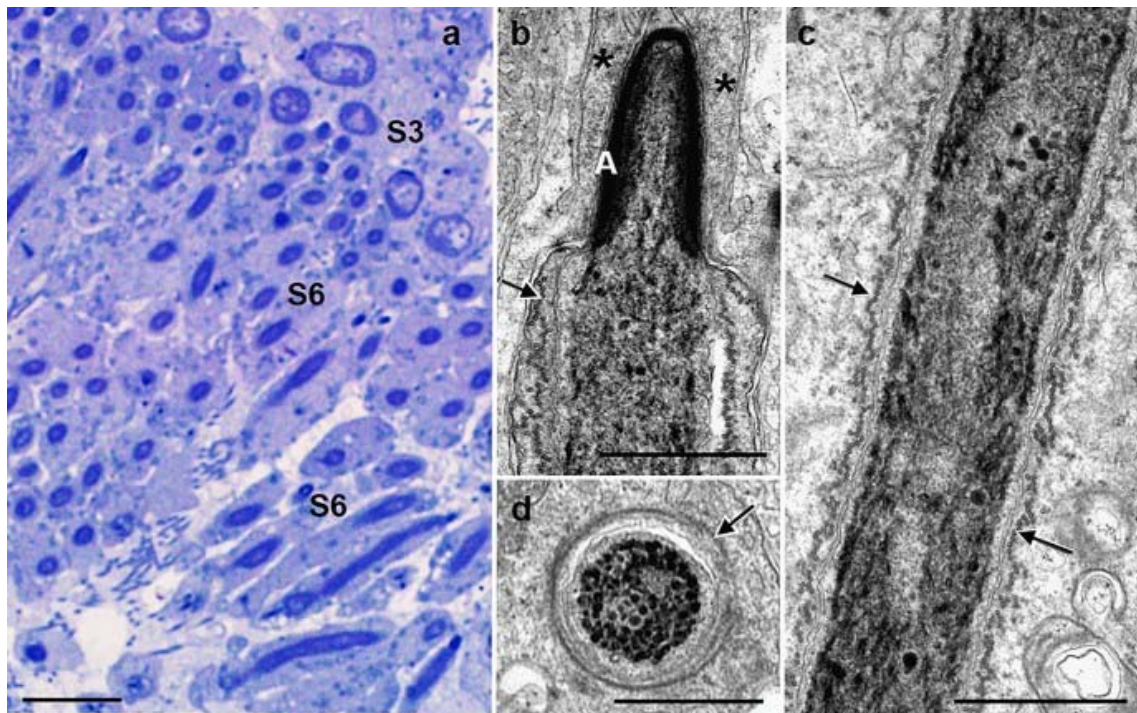

Fig. 8. Step 6 spermatids. **a** Light micrographs showing an extensive layer of spermatids (S6) in both transverse and longitudinal section. Note the typical dark periphery and lighter centers of the nuclei. A group of step 3 spermatids (S3) is also present. **b**–**d** TEM showing longitudinal (**b**, **c**) and transverse (**d**) spermatid profiles. Note the conical acrosome (A), the finely granular central material and peripheral fibrils in the nucleus, and the circular manchette (arrows). Asterisks in panel **b** mark Sertoli cell cytoplasm. Bars **a** = 5 μm, **b**–**d** = 1 μm
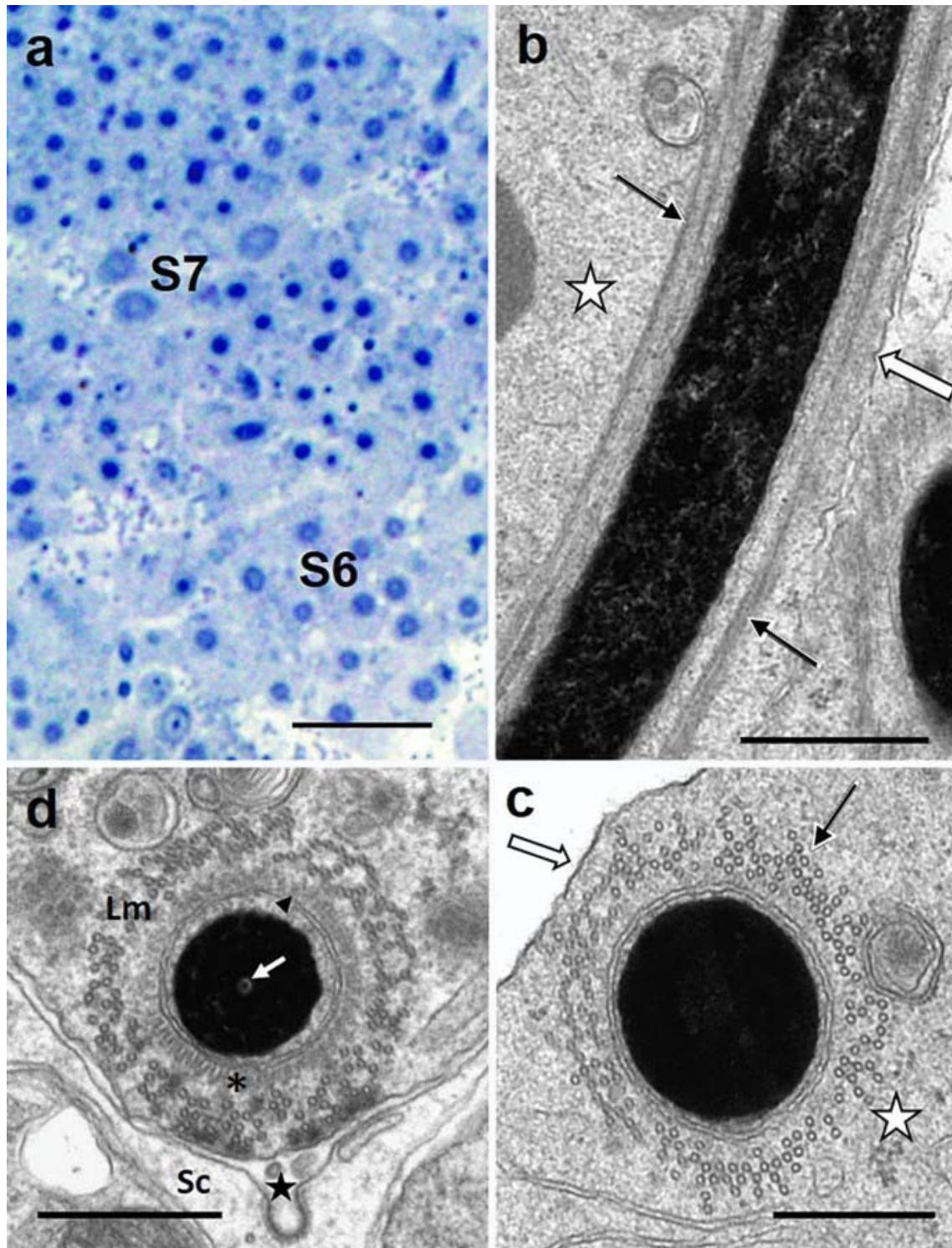
Fig. 9. a A group of step 7 spermatids (S7) in transverse profile. The nuclei are narrower than those of step 6 spermatids (S6) and stain darker and reveal only a minute pale center. **b** and **c** TEM showing longitudinal and transverse profiles of a step 7 spermatid, respectively. Note the advanced stage of peripheral chromatin compaction and looser central configuration and the microtubules of the longitudinal manchette (arrows). The residual cytoplasm is eccentrically positioned (white stars). Plasma membrane (open arrows). **d** Transverse section of a slightly earlier step 7 spermatid sectioned more proximally to that illustrated in Fig. 7c, showing the endonuclear canal containing the acrosomal rod (arrow). The finger-like array (asterisk) situated between the nuclear membrane (arrowhead) and

the microtubules of the longitudinal manchette (Lm) is partially obvious due to the plane of section. A coated pit (star) is present on the surface of a surrounding Sertoli cell (Sc). Bars **a** = 5 μm, **b** = 1 μm, **c** = 0.5 μm, **d** = 0.5 μm

Step 7

This phase was characterized by further elongation and narrowing of the nucleus (0.84 ± 0.02 μm in diameter). An accurate assessment of nuclear length was not possible due to a lack of complete longitudinal profiles in the sections examined. The karyoplasm stained intensely although a minute pale center could be observed in transverse sections of some early step 7 cells (Fig. 9a). The acrosome was similar in appearance to that seen in step 6 spermatids. TEM revealed highly compacted nuclear contents with a looser arrangement toward the center of the nucleus, confirming the LM observations (Fig. 9b, c). During this step, a well-developed longitudinal manchette was apparent in contrast to the circular manchette that characterized step 3 to 6 spermatids (Fig. 9b, c). An extensive array of finger-like projections, first present as isolated, randomly distributed structures during the development of the circular manchette, was observed between the longitudinal manchette and the nuclear envelope (Fig. 9d). Toward the end of this phase, the projections were observed to abruptly disappear, followed by the gradual dissolution of the longitudinal manchette (see (du Plessis and Soley 2013, 2016)). The residual cytoplasm in the head region adopted an eccentric position relative to the nucleus and surrounding longitudinal manchette (Fig. 9b, c).
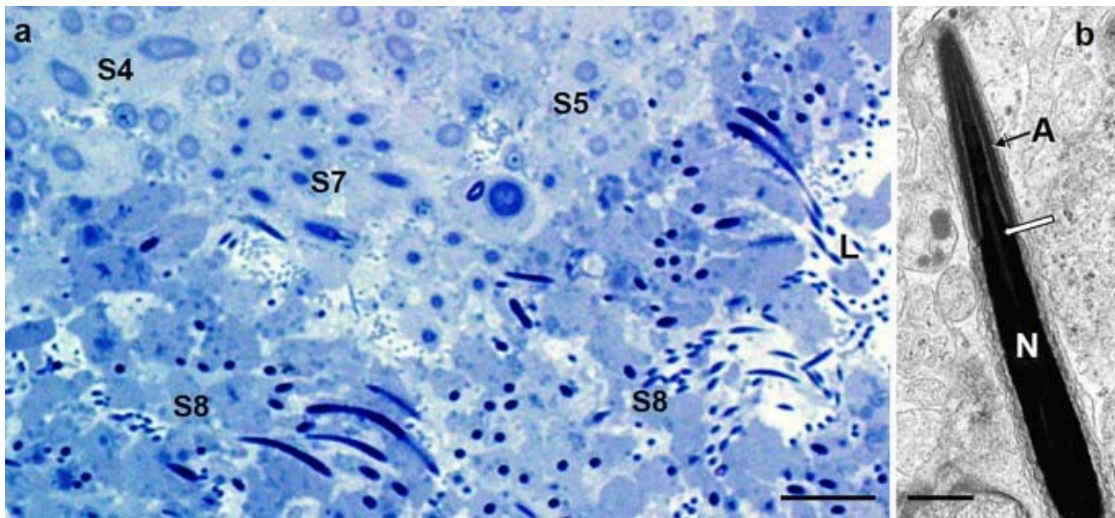

Fig. 10. a A layer of step 8 (S8) spermatids lies adjacent to the tubular lumen (L). Step 4 (S4), step 5 (S5), and step 7 (S7) spermatids are also present. Note the narrow, intensely stained nucleus and dark-staining residual cytoplasm of step 8 S* spermatids. **b** TEM of the apical aspect of the head of a step 8 spermatid in longitudinal profile. The acrosome (A) and nucleus (N) are tightly bound by the plasma membrane. Chromatin compaction is complete, and the endonuclear canal can be faintly seen at the center of the nucleus (white arrow). Bars **a** = 5 μm, **b** = 1 μm

Step 8

Step 8 spermatids were positioned adjacent to the tubular lumen and typically displayed a narrow (diameter of 0.66 ± 0.04 μm), intensely stained nucleus and conical acrosome. The residual cytoplasm of these cells was darker staining than that of the other steps (Fig. 10a) and, in fortuitously sectioned cells, was seen to concentrate toward the base of the nucleus and the

midpiece of the tail. The tails extended into the tubular lumen where they were surrounded by residual bodies. Complete compaction of the nuclear contents was observed by TEM, and the longitudinal manchette was absent (Fig. 10b).

Imaging of sperm head shaping and acrosomal biogenesis

The PNA staining of the acrosome was observed for the first three steps of spermiogenesis. Based on PNA staining, step 1 spermatids could be divided into two relatively distinct groups: (a) round spermatids with scattered foci of positive staining material presumed to represent pro-acrosomal granules (Fig. 11a) and (b) cells with a single, conspicuous, round structure positioned close to, but not in contact with, the nuclear surface (Fig. 11b). This structure was considered to represent the consolidated elements of the pre-acrosomal granules (the acrosomal granule surrounded by elements of the Golgi complex) or the finally formed acrosomal vesicle containing dissipated elements of the granule. This distinction could not accurately be made by LM, thus the consolidation of both morphological characteristics within a single step. In step 2 spermatids, the acrosomal granule/vesicle, still spherical in shape, was positioned in close contact with the nuclear envelope (Fig. 11c), generally within a shallow concave depression. During step 3, the acrosomal vesicle was observed to have collapsed forming a flattened, sometimes slightly convex cap at the apex of the spermatid nucleus which demonstrated one or more constrictions (Fig. 11d–f) and occasionally showing the apical bulging of the nucleus as it seemed to partially separate from the manchette (Fig. 11g, h). From step 4 onwards, the acrosome, clearly crescent-shaped in step 4 and progressively more conical-shaped from step 5 to step 8 (based on routine LM and TEM), failed to take up the lectin stain (Fig. 11i) as did epididymal (Fig. 11j) and ejaculated spermatozoa (Fig. 11k).

Tubulin, by virtue of anti-tubulin antibody labeling of both microtubules and monomeric cytosolic tubulin, was diffusely spread throughout the cytoplasm in step 1 and step 2 spermatids (Fig. 11a–c). In step 3 to step 7 spermatids, the tubulin was consolidated into a distinct layer around the nucleus, following the nuclear contours (Fig. 11d–g). This layer of tubulin represented the microtubules of the circular (steps 3 to 6) and longitudinal (step 7) manchette observed by TEM. This phenomenon was not observed in step 8 spermatids (absence of manchette microtubules) and post-testicular spermatozoa. However, tubulin was detected throughout the length of the developing flagellum in spermatids and post-testicular spermatozoa, particularly in the tail midpiece, due to the presence of axonemal and centriolar microtubules (the long distal centriole of ratites forms the core of the entire midpiece) (Fig. 11h, i). An interesting phenomenon was the lack of tubulin staining around the apex of the nucleus which first became apparent in step 3 spermatids (Fig. 11d–f).
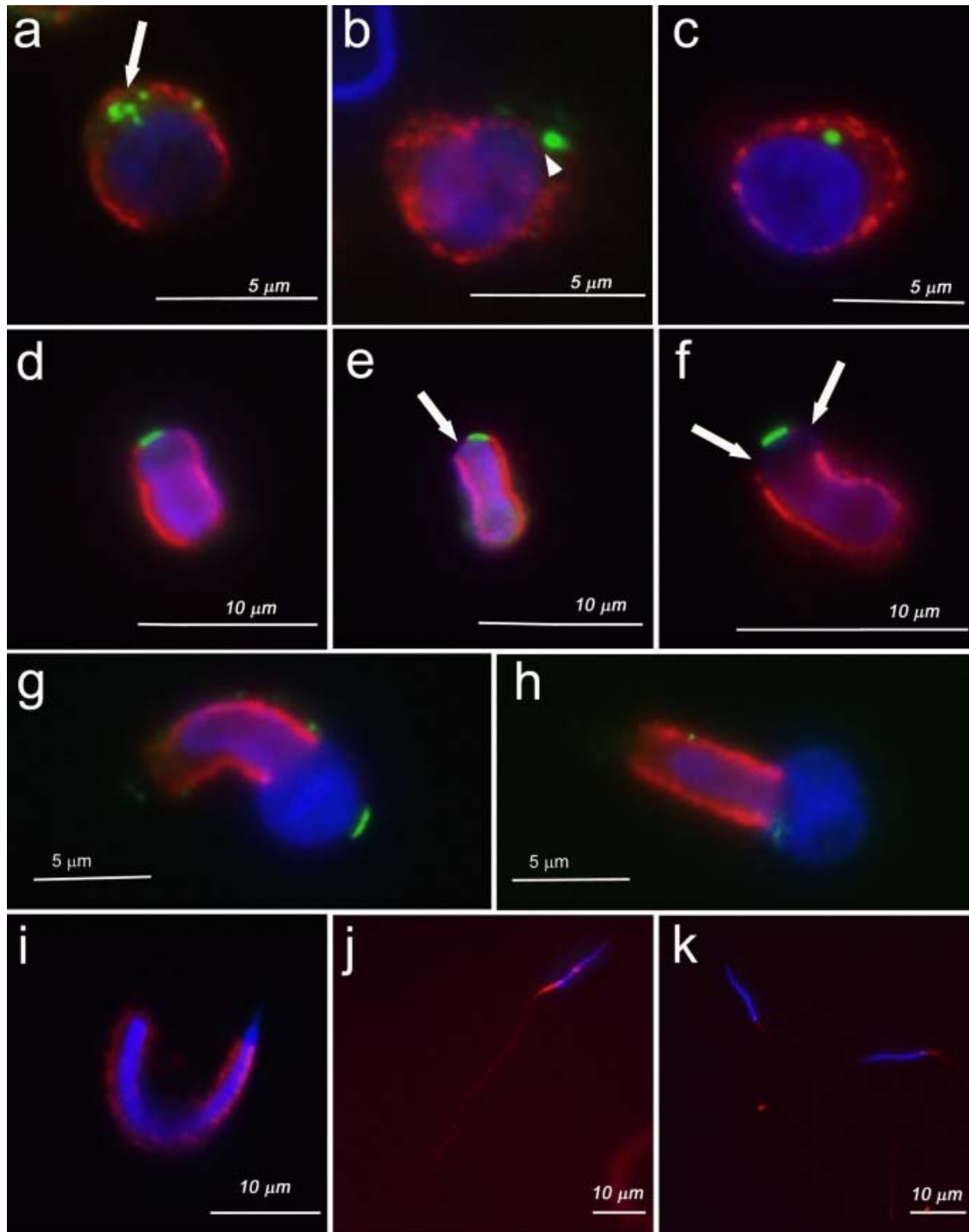
Fig. 11. Isolated spermatogenic cells illustrating the early stages in the formation of the acrosome (green color) after PNA staining. Concurrent immunofluorescent staining shows the nuclear contents in blue and tubulin beta (TUBB) in red. **a**, **b** Step 1 spermatids. The cell in (**a**) illustrates the earliest step characterized by the presence of scattered pro-acrosomal granules (arrow) whereas in (**b**) a single acrosomal vesicle has formed but is not yet attached to the nuclear membrane. Note the obvious gap between the vesicle and the nucleus (arrowhead). **c** Step 2 spermatid. The acrosomal vesicle lies nestled in a concave depression of the nuclear envelope although on LM, the indentation is not always as obvious as seen by TEM. Tubulin is diffusely scattered in the cytoplasm of step 1 and 2 spermatids. **d**–**f** Step 3 spermatids. The acrosomal vesicle, now flattened, lies at the apex of the nucleus which appears

18

constricted. The tubulin is concentrated around the nucleus beneath the acrosome, forming the circular manchette observed by TEM. Note the apparent progressive retreat (or lack of formation) of the circular manchette from the tip of the nucleus immediately beneath the forming acrosome (arrows). **g**, **h** Typical examples of the nuclear bulging observed beneath the forming acrosome in some isolated step 3 spermatids. **i** A step 5 or 6 spermatid identified by the pointed tip of the nucleus. The acrosome is not observed due to the lack of PNA labeling. The circular manchette, indicated by positive tubulin staining, extends the length of the nucleus. Epididymal (**j**) and ejaculated (**k**) spermatozoa, respectively. Tubulin labeling is confined to the flagellum (indicating the microtubules of the axoneme) and is particularly obvious in the midpiece, possibly indicating greater permeability of this part of the sperm tail to the stain or to the presence of the nine sets of triplet microtubules embedded in the walls of the distal centriole that typically extends the length of the midpiece in ratites (Baccetti et al. 1991; du Plessis and Soley 2014; Soley 1993) and the tinamou (Asa et al. 1986). The consistent hint of tubulin labeling at the base of the nucleus and sperm tail midpiece in both epididymal and ejaculated spermatozoa may indicate the presence of tubulin in a non-polymerized form following dissolution of the longitudinal manchette during the final stages of spermiogenesis, or as mentioned above, to the detection of tubulin in the elongated distal centriole

Discussion

Unlike in mammals, determining the stages of the cycle of the seminiferous epithelium, i.e., the cellular associations that characterize spermatogenesis, has proved to be a contentious exercise in the avian seminiferous epithelium. According to some authors, no pattern of germ cell associations could be discerned in the fowl, guinea fowl, or turkey (Noirault et al. 2006), a situation also reported in the quail (Yamamoto et al. 1967). This lack of clarity in recognizing such associations has been ascribed to the presence in the epithelium of atypical stages (Aire et al. 1980; Clermont 1958; Yamamoto et al. 1967) as well as the relatively quick transition occurring between certain germ cell categories (Lake 1981). In contrast, other studies have documented specific cellular associations in birds, with eight stages (Yamamoto et al. 1967) or ten stages (Lin et al. 1990) of the cycle of the seminiferous epithelium being described in the quail, 8 (Aire et al. 1980) or 9 (Abdul-Rahman et al. 2017) in the guinea fowl, and 9 in the goose (Akhtar et al. 2020). It was clear from the present study that some parts of the seminiferous tubules presented an orderly arrangement of the specific germ cell types in the epithelium, while in other parts a more disorganized pattern, characterized by a degree of intermingling of cell types/developmental stages, was apparent. Whether this is a normal phenomenon in the ostrich or possibly an impression accentuated by the plane of section remains unknown.

In contrast to what has generally been reported in birds (see "Introduction"), only 8 steps of spermiogenesis could be identified by light microscopy in the ostrich based on changes in nuclear shape and appearance of the chromatin, the positioning of the centriolar complex, and on acrosome development. Compounding the difficulty in assigning additional steps to ostrich spermatid development during the early stages is the ubiquitous presence of cytoplasmic vacuoles and densities observed during this period of development, the limited chance of seeing definitive structural features, even in a group of sectioned cells, and the occurrence of atypical cellular associations. Thus, only two steps could be recognized with certainty during the round spermatid steps of development, with the first step encompassing the formation of the acrosome granule and subsequent acrosomal vesicle (Soley 1996) and the second step involving the attachment of the acrosomal vesicle (and the centriolar complex) to the nuclear envelope. Collectively, most studies in birds identify between 4 and 5 steps reflecting changes to the round spermatids (Aire 2003; Aire et al. 1980; Clermont 1958; Gunawardana 1977; Lin and Jones 1993; Lin et al. 1990), although as many as 7 steps have been illustrated for the fowl

(Cavazos and Melampy 1954). These changes are centered around the origin, location, and eventual attachment of the acrosomal vesicle to the nuclear envelope, features that are not observed in the ostrich testis when employing light microscopy and toluidine blue staining. Based on these observations, step 1 spermatids, as defined in the present study, may very well reflect developmental stages additionally mentioned by other authors. This is substantiated by the observation that the flagellum only appears to originate from step 2 in some studies (Aire 2003; Gunawardana and Scott 1977; Lin et al. 1990), whereas it is already present in step 1 spermatids in the current investigation. Likewise, in the ostrich, the nucleus of round spermatids, as also reported in the fowl (Sprando and Russell 1988) and in the sparrow (Goes and Dolder 2002), only displays two forms in respect of its contents, unlike the progression of chromatin changes described or illustrated in other reports (Aire 2003; Aire et al. 1980; Gunawardana 1977; Lin and Jones 1993; Lin et al. 1990). A consistent finding in all of the studies, however, including the present, is the peripheral accumulation of the chromatin along the inner aspect of the nuclear envelope during the round spermatid phase of development (Aire 2003; Aire et al. 1980; Gunawardana 1977; Lin et al. 1990; Sprando and Russell 1988). The present study reveals lectin labeling of the nascent acrosome as an additional criterion that is informative of the distinct spermatid elongation steps. Lectin PNA staining of the acrosome which is confined to the initial three steps of spermiogenesis (elaborated on below) was clearly demonstrated by using this technique.

Most studies agree regarding a specific step when the round nucleus of the early spermatid adopts a typical pear-shaped or irregular appearance that reflects the start of the elongation process of the developing spermatid. Owing to the limited number of round spermatid steps recognized in the ostrich, this transformation in nuclear shape occurs during step 3, as has also been described in the Barbary duck (Marchand 1977) and rooster (Sprando and Russell 1988). In other studies, it occurs later, appearing during step 5 in the turkey (Aire 2003), guinea fowl (Aire et al. 1980), and domestic fowl (Gunawardana 1977) and step 6 in the Japanese quail (Lin and Jones 1993; Lin et al. 1990). Uniquely, in the ostrich, this step demonstrates two forms in respect of the nuclear contents, the first appearing like that of step 2 spermatids and considered here to represent the initial transition from step 2 to step 3 and a second form with homogeneous nuclear contents. Despite the difference in appearance of the nuclear contents, both forms were designated as step 3 spermatids in this study. Thereafter, in all species, the spermatids show a reduction in nuclear diameter, lengthening of the nucleus, and concomitant condensation of the chromatin. Transition from the initial change in nuclear shape until complete compaction of the chromatin prior to spermiation involves 6 steps in the ostrich, similar to that reported in the fowl (Gunawardana 1977) and Guinea fowl (Aire et al. 1980). However, varying numbers of steps have also been presented for this sequence of changes, with 5 steps noted in the fowl (Sprando and Russell 1988), 7 in the Japanese quail (Lin and Jones 1993; Lin et al. 1990), and 8 in the turkey (Aire 2003). The literature reveals broad consensus in respect of the sequence of changes that take place during spermiogenesis in birds (for a detailed comparative discussion on avian spermiogenesis, including ratites, see (Aire 2007, 2014, 2018; du Plessis and Soley 2013, 2016; Soley 1994, 1996, 1997)). The differences that are recorded for the number of steps characterizing this process reflect the amount of detail that can be (is) observed or that is recognized as being practical by the authors. In the ostrich material studied, for example, the cytoplasmic events that occur during the round spermatid stage of development can be divided into several steps by using ultrastructural data (Soley 1994, 1996, 1997). However, as outlined above, the same detail cannot consistently be observed by LM unless lectin labeling of acrosomal precursors is applied, resulting in only two steps being obvious based on general cytoplasmic features and nuclear characteristics. It would be tempting, for example, to assign an earlier step in spermiogenesis based on a lack of pro-

acrosomal granules in the cytoplasm. Likewise, step 3 spermatids could be divided into two separate steps based on the change in nuclear contents that occurs, but such subtleties reflect a transitional development and not necessarily an independent step.

A number of studies in mammals (Bains et al. 1992; Nakata et al. 2017) have indicated that lectins, in particular peanut agglutinin (PNA), can be used as sperm acrosome-specific markers and consequently have value in identifying specific developmental stages of spermatids based on the structure of the acrosome (Nakata et al. 2015; Wakayama et al. 2015). Studies on the mouse testis also showed that PNA specifically stains the outer membrane and contents of the acrosome in the fully differentiated spermatozoon and detects the pro-acrosomal granule in the early step round spermatids, as well as the acrosomal cap in later step round spermatids and elongating spermatids (Nakata et al. 2015; Wakayama et al. 2015). Such acrosomal structure staining is commonly performed in fixed and permeabilized whole sperm or spermatid mounts and on testicular tissue sections. As the PNA-binding acrosomal components are concealed by the overlying plasma membrane in mature spermatozoa, lectin PNA can be used to screen live spermatozoa for acrosomal damage or exocytosis in a variety of mammalian species (Sutovsky et al. 2015). However, varying results have been achieved with the use of PNA in labeling the avian acrosome. In a study of cell types in the seminiferous epithelium (SE) of the sexually mature turkey (Bakst et al. 2007), using a variety of lectins, only PNA reacted with the germ cell component. However, this was restricted to spermatogonia and leptotene spermatocytes with the authors noting that "spermatids, regardless of the stage of spermiogenesis, either failed to stain or possessed minor affinity to PNA." Similarly, no cell type in the SE of the mature chicken testis displayed affinity for PNA (Bakst et al. 2007), and the acrosome of duck spermatozoa also failed to react with PNA (Majhi et al. 2016). Moreover, spermatogenic cells in the cock testis were observed to exhibit weak reactivity with PNA (Keskin and Ili 2011). However, other studies on chicken spermatozoa (Ashizawa et al. 2006; Horrocks et al. 2000; Robertson and Wishart 1996) revealed that PNA fails to bind to acrosome-intact spermatozoa but does bind to acrosome-reacted spermatozoa. Compounding this ambiguity, a study characterizing the glycocalyx of chicken and turkey spermatozoa found that morphologically normal spermatozoa stained in suspension with PNA were "basically unstained in both non-treated and neuraminidase-treated samples," although detached acrosomes showed bright fluorescence (Pelaez and Long 2007). However, when spermatozoa were fixed, air-dried, and incubated with PNA, binding to the head and acrosome was observed. These variable results would seem to suggest that sample preparation and experimental methodology play a role in this avian-specific phenomenon, which agrees with the absence of acrosomal PNA stainability beyond the initial steps of ratite spermiogenesis reported in the present study. Other lectins tested in the study failed to detect acrosomal caps/acrosomes in tissue sections or whole mount cell samples. These included *Griffonia simplicifolia* lectin/GSA, *Canavalia ensiformis*/Concanavalin A/ConA, *Lens culinaris* agglutinin/LCA, *Lotus tetragonolobus* lectin/LTL, *Phaseolus vulgaris* phytohemagglutinin/PHA-P, and *Ricinus communis* agglutinin/RCA. Thus, in the ostrich, the only lectin that displayed acrosome reactivity from the selection employed was PNA and only for the first three steps of spermiogenesis. The forming acrosome of round spermatids showed strong staining with PNA, from the formation of pro-acrosomal granules/vesicles to formation and attachment of the acrosomal vesicle to, and its initial extension around the tip of the nucleus. These early stages of acrosome formation have also been identified in the urodele amphibian, *Triturus marmoratus*, by using a lectin derived from the snail *Helix pomatia* (HPA) which stains the acrosome at all stages of spermiogenesis (Valbuena et al. 2008). Following step 3 of spermiogenesis in the ostrich (defined by the presence of a flattened, sometimes slightly convex, acrosome), acrosome affinity for PNA abruptly ended. This loss of PNA labeling may

be due to a number of factors, for example, a change in the composition of the PNA-reactive glycoconjugates in later stage spermatids or a change in the "process of compaction and storage of the acrosomal contents" (Valbuena et al. 2008). Further studies employing other lectins may provide some clarity on this topic. However, PNA labeling of both isolated spermatogenic cells and testis sections provided corroborating evidence relative to the earlier phases of acrosome development in the ostrich.

Immunocytochemical labeling of isolated spermatogenic cells in the ostrich revealed an interesting phenomenon in respect of acrosome formation. It was observed in some spermatids that the forming nuclear manchette (reactive for tubulin) appeared to retreat from the nuclear region just beneath the forming acrosome. This would agree with an earlier study (Soley 1996) which suggested that the tip of the nucleus in ostrich spermatids is shaped by the forming acrosome and not by the manchette. Retreat of the manchette microtubules from the immediate vicinity of the forming acrosome would enable this process to occur. The nuclear bulging observed beneath the forming acrosome in some isolated cells may be an indication of the retreat of the manchette microtubules from the region of the spermatid cytoplasm around that part of the nucleus destined to be covered by the expanding acrosome, resulting in a temporary weakness through which the nucleus, no longer constrained by the manchette, swells through the gap.

It is concluded that spermiogenesis in the ostrich follows the general pattern described for non-passerine birds. While conceding that more steps of spermiogenesis could theoretically be described for this species by using a combination of light and electron microscopy, supplemented by various histochemical stains and lectin labeling, only 8 steps were recognized with certainty by light microscopy of toluidine blue-stained plastic sections. The observation that PNA was the only lectin to label the forming acrosome, and only for the initial three steps of spermiogenesis, suggests that the acrosomal contents have a specific configuration and/or constituency that changes (modifies) as development proceeds. This phenomenon merits further investigation.

Funding

Ethics declarations

Conflict of interest

The authors declare no competing interests.

Ethical approval

This article does not contain any studies with human participants or animals performed by any of the authors.

References

Abdul-Rahman I, Obese F, Robinson J (2017) Spermatogenesis and cellular associations in the seminiferous epithelium of Guinea cock (Numida meleagris). Can J Anim Sci 97:241–249

Aire TA (2003) Ultrastructural study of spermiogenesis in the turkey, Meleagris gallopavo. Br Poult Sci 44:674–682

Aire TA (2007) Spermatogenesis and testicular cycles. In: Jamieson BMG (ed) Reproductive Biology and Phylogeny of Birds, vol 6A Science Publishers, Jersey, pp 279–347

Aire TA (2014) Spermiogenesis in birds. Spermatogenesis 4:e959392

Aire TA (2018) Spermatogenesis and spermiogenesis, birds. Encyclopedia of Reproduction 6:313–320

Aire TA, Olowo-okorun MO, Ayeni JS (1980) The seminiferous epithelium in the guinea fowl (Numida meleagris). Cell Tissue Res 205:319–325

Akhtar MF, Ahmad E, Mustafa S, Chen Z, Shi Z, Shi F (2020) Spermiogenesis, stages of seminiferous epithelium and variations in seminiferous tubules during active states of spermatogenesis in Yangzhou goose ganders. Animals (Basel) 10

Asa C, Philips DM, Stover J (1986) Ultrastructure of spermatozoa of the crested tinamou. J Ultra Mol Struct R 94:170–175

Ashizawa K, Wishart GJ, Katayama S, Takano D, Ranasinghe AR, Narumi K, Tsuzuki Y (2006) Regulation of acrosome reaction of fowl spermatozoa: evidence for the involvement of protein kinase C and protein phosphatase-type 1 and/or -type 2A. Reproduction 131:1017–1024

Baccetti B, Burrini AG, Falchetti E (1991) Spermatozoa and relationships in Palaeognath birds. Biol Cell 71:209–216

Bains HK, Sehgal S, Bawa SR (1992) Human sperm surface mapping with lectins. Acta Anat (basel) 145:207–211

Bakst MR, Akuffo V, Trefil P, Brillard JP (2007) Morphological and histochemical characterization of the seminiferous epithelial and Leydig cells of the turkey. Anim Reprod Sci 97:303–313

Barth AD, Oko RJ (1989) Abnormal morphology of bovine spermatozoa. Iowa State University Press, Ames, IA

Bonato M, Rybnik PK, Malecki IA, Cornwallis CK, Cloete SWP (2011) Twice daily collection yields greater semen output and does not affect male libido in the ostrich. Anim Reprod Sci 123:258–264

Cavazos LF, Melampy RM (1954) A comparative study of periodic acid-reactive carbohydrates in vertebrate testes. Am J Anat 95:467–495

Clermont Y (1958) Structure of the epithelium of the seminiferous tubules and the mechanism of regeneration of the spermatogonia in the duck. Arch Anat Microsc Morphol Exp 47:47–66

Clermont Y, Leblond CP (1955) Spermiogenesis of man, monkey, ram and other mammals as shown by the periodic acid-Schiff technique. Am J Anat 96:229–253

Clermont Y, Rambourg A (1978) Evolution of the endoplasmic reticulum during rat spermiogenesis. Am J Anat 151:191–211

Cloete SWP, Brand Z, Bunter KL, Malecki IA (2008) Direct responses in breeding values to selection of ostriches for liveweight and reproduction. Aust J Exp Agr 48:1314–1319

Courtens JD, A, (1985) Spermiogenesis of Lacerta vivipara. J Ultrastruct Res 90:203–220

du Plessis L, Soley JT (2013) A novel transient structure with phylogenetic implications found in ratite spermatids. BMC Evol Biol 13:104

du Plessis L, Soley JT (2014) A re-evaluation of sperm ultrastructure in the emu, Dromaius novaehollandiae. Theriogenology 81:1073–1084

du Plessis L, Soley JT (2016) Sperm head shaping in ratites: new insights, yet more questions. Tissue Cell 48:605–615

Fawcett DW, Phillips DM (1969) The fine structure and development of the neck region of the mammalian spermatozoon. Anat Rec 165:153–164

Ferreira A, Dolder H (2003) Sperm ultrastructure and spermatogenesis in the lizard, Tropidurus itambere. Biocell 27:353–362

Goes RM, Dolder H (2002) Cytological steps during spermiogenesis in the house sparrow (Passer domesticus, Linnaeus). Tissue Cell 34:273–282

Gribbins KM (2011) Reptilian spermatogenesis: a histological and ultrastructural perspective. Spermatogenesis 1:250–269

Gunawardana VE (1977) Stages of spermatids in the domestic fowl: a light microscope study using Araldite sections. J Anat 123:351–360

Gunawardana VK, Scott MG (1977) Ultrastructural studies on the differentiation of spermatids in the domestic fowl. J Anat 124:741–755

Holstein AF (1976) Ultrastructural observations on the differentiation of spermatids in man. Andrologia 8:157–165

Holt WV, Moore HD (1984) Ultrastructural aspects of spermatogenesis in the common marmoset (Callithrix jacchus). J Anat 138(Pt 1):175–188

Horrocks AJ, Stewart S, Jackson L, Wishart GJ (2000) Induction of acrosomal exocytosis in chicken spermatozoa by inner perivitelline-derived N-linked glycans. Biochem Biophys Res Commun 278:84–89

Jones RC, Lin M (1993) Spermatogenesis in birds. Oxf Rev Reprod Biol 15:233–264

Kawka M, Horbanczuk JO, Sacharczuk M, Zieba G, Lukaszewicz M, Jaszczak K, Parada R (2007) Genetic characteristics of the ostrich population using molecular methods. Poultry Sci 86:277–281

Keskin N, Ili P (2011) Glycohistochemical study on the Denizli cock testis. J Anim Vet Adv 10:1327–1331

Lake PE (1981) Male genital organs. In: King AS, McLelland J (eds) Form and function in birds, vol 2. Academic Press, London, pp 2–61

Lambrechts H, Swart D, Cloete SWP, Greyling JPC, van Schalkwyk SJ (2004) The influence of stocking rate and male : female ratio on the production of breeding ostriches (Struthio camelus spp.) under commercial farming conditions. S Afr J Anim Sci 34:87–96

Leblond CP, Clermont Y (1952) Spermiogenesis of rat, mouse, hamster and guinea pig as revealed by the periodic acid-fuchsin sulfurous acid technique. Am J Anat 90:167–215

Lin M, Jones RC (1993) Spermiogenesis and spermiation in the Japanese quail (Coturnix coturnix japonica). J Anat 183:525–535

Lin M, Jones RC (2000) Spermiogenesis and spermiation in a monotreme mammal, the platypus, Ornithorhynchus anatinus. J Anat 196:217–232

Lin M, Jones RC, Blackshaw AW (1990) The cycle of the seminiferous epithelium in the Japanese quail (Coturnix coturnix japonica) and estimation of its duration. J Reprod Fertil 88:481–490

Lovas EM, Filippich LJ, Johnston SD (2012) Spermiogenesis in the Australian cockatiel Nymphicus hollandicus. J Morphol 273:1291–1305

Majhi RK, Kumar A, Yadav M, Kumar P, Maity A, Giri SC, Goswami C (2016) Light and electron microscopic study of mature spermatozoa from White Pekin duck (Anas platyrhynchos): an ultrastructural and molecular analysis. Andrology 4:232–244

Malecki IA, Rybnik PK, Martin GB (2008) Artificial insemination technology for ratites: a review. Aust J Exp Agr 48:1284–1292

Manandhar G, Sutovsky P (2007) Comparative histology and subcellular structure of mammalian spermatogenesis and spermatozoa. In: Schatten H (ed) Comparative Reproductive Biology pp 81–98

Marchand CR (1977) Ultrastructural study of the spermatogenesis of the Barbary drake (Cairina moschata L. Aves. Anatidae). Biol Cell 29:193–202

Mattei C, Mattei X, Manfredi J (1972) Electron microscope study of the spermiogenesis of Streptopelia roseogrisea. J Submicrosc Cytol 4:57–73

Nakata H, Wakayama T, Asano T, Nishiuchi T, Iseki S (2017) Identification of sperm equatorial segment protein 1 in the acrosome as the primary binding target of peanut agglutinin (PNA) in the mouse testis. Histochem Cell Biol 147:27–38

Nakata H, Wakayama T, Takai Y, Iseki S (2015) Quantitative analysis of the cellular composition in seminiferous tubules in normal and genetically modified infertile mice. J Histochem Cytochem 63:99–113

Noirault J, Brillard JP, Bakst MR (2006) Spermatogenesis in the turkey (Meleagris gallopavo): quantitative approach in immature and adult males subjected to various photoperiods. Theriogenology 65:845–859

Pelaez J, Long JA (2007) Characterizing the glycocalyx of poultry spermatozoa: I. Identification and distribution of carbohydrate residues using flow cytometry and epifluorescence microscopy. J Androl 28:342–352

Ricci M, Breed WG (2005) Morphogenesis of the fibrous sheath in the marsupial spermatozoon. J Anat 207:155–164

Robertson L, Wishart GJ (1996) Detection of the acrosome reaction of chicken spermatozoa. J Reprod Fertil Abstr Ser 17:115

Saita A, Comazzi M, Perrotta E (1987) Electron microscope study of spermiogenesis in Caiman crocodylus L. Ital J Zool 54:307–318

Setchell BP, Carrick FN (1973) Spermatogenesis in some Australian marsupials. Aust J Zool 21:491–499

Simoes K, Orsi AM, Viegas KA (2005) Ultrastructural characteristics of spermiogenesis in the domestic duck (Anas platyrhynchos). Anat Histol Embryol 34:307–311

Soley JT (1993) Ultrastructure of ostrich (Struthio camelus) spermatozoa: I. Transmission electron microscopy. Onderstepoort J Vet Res 60:119–130

Soley JT (1994) Centriole development and formation of the flagellum during spermiogenesis in the ostrich (Struthio camelus). J Anat 185:301–313

Soley JT (1996) Differentiation of the acrosomal complex in ostrich (Struthio camelus) spermatids. J Morphol 227:101–111

Soley JT (1997) Nuclear morphogenesis and the role of the manchette during spermiogenesis in the ostrich (Struthio camelus). J Anat 190:563–576

Soley JT, Groenewald HB (1999) Reproduction. In: Deeming DC (ed) The Ostrich: Biology, Production and Health. CABI Publishing, Oxon, pp 129–158

Sprando RL, Russell LD (1988) Spermiogenesis in the red-ear turtle (Pseudemys scripta) and the domestic fowl (Gallus domesticus): a study of cytoplasmic events including cell volume changes and cytoplasmic elimination. J Morphol 198:95–118

Sutovsky P (2004) Visualization of sperm accessory structures in the mammalian spermatids, spermatozoa, and zygotes by immunofluorescence, confocal, and immunoelectron microscopy. Methods Mol Biol 253:59–77

Sutovsky P, Aarabi M, Miranda-Vizuete A, Oko R (2015) Negative biomarker based male fertility evaluation: sperm phenotypes associated with molecular-level anomalies. Asian J Androl 17:554–560

Sutovsky P, Manandhar G, McCauley TC, Caamano JN, Sutovsky M, Thompson WE, Day BN (2004) Proteasomal interference prevents zona pellucida penetration and fertilization in mammals. Biol Reprod 71:1625–1637

Valbuena G, Hernandez F, Madrid JF, Saez FJ (2008) Acrosome biosynthesis in spermatocytes and spermatids revealed by HPA lectin cytochemistry. Anat Rec 291:1097–1105

Wakayama T, Nakata H, Kumchantuek T, Gewaily MS, Iseki S (2015) Identification of 5-bromo-2'-deoxyuridine-labeled cells during mouse spermatogenesis by heat-induced antigen retrieval in lectin staining and immunohistochemistry. J Histochem Cytochem 63:190–205

Yamamoto S, Tamate H, Itikawa O (1967) Morphological studies on the sexual maturation in the male Japanese quail (Coturnix coturnix japonica). II. The germ cell types and cellular associations during spermatogenesis. Tohoku J Ag Res 18:27–39

Yasuzumi F, Yamaguchi S (1977) Some aspects of spermiogenesis in the domestic pigeon. Okajimas Folia Anat Jpn 54:139–174

Yi YJ, Manandhar G, Sutovsky M, Li R, Jonakova V, Oko R, Park CS, Prather RS, Sutovsky P (2007) Ubiquitin C-terminal hydrolase-activity is involved in sperm acrosomal function and anti-polyspermy defense during porcine fertilization. Biol Reprod 77:780–793